Full length article

Local droplet etching of a vicinal InGaAs(111)A metamorphic layer

Artur Tuktamyshev [a,b,*], Davide Lambardi [a,b], Stefano Vichi [a,b], Federico Cesura [a,b], Stefano Cecchi [a,b], Alexey Fedorov [b,c], Sergio Bietti [a,b], Stefano Sanguinetti [a,b]

[a] *Bicocca Quantum Technologies (BiQuTe) center and Materials Science Department, University of Milano-Bicocca, via R. Cozzi 55, Milano, 20126, Italy*
[b] *Laboratory for Nanostructure Epitaxy and Spintronics on Silicon (L-NESS), via F. Anzani 42, Como, 22100, Italy*
[c] *The National Research Council - Institute for Photonics and Nanotechnologies (CNR-IFN), piazza Leonardo da Vinci 32, Milano, 20133, Italy*

ARTICLE INFO

ABSTRACT

We demonstrated nanopit formation by Ga-assisted local droplet etching technique in InGaAs metamorphic layers grown on vicinal GaAs(111)A substrates. We studied nanopit formation depending on the substrate temperature, Ga flux and Ga amount. The etched pits show a highly symmetrical pyramidal shape with an equilateral triangular base and the edges of the triangle are along $< 1\bar{1}0 >$ directions. The observed behavior, in terms of nanopit density, depth and, aspect ratio is well described by a model taking into account the dynamics of the droplet etching process.

1. Introduction

In the ongoing pursuit of practical quantum technologies, a critical focus is developing a deterministic and efficient quantum source of entangled photons. Such a source is pivotal in quantum communication protocols and certain quantum simulation applications [1,2]. Notably, their development is essential for the realization of repeaters capable of transferring quantum entanglement over long distances.

Epitaxial quantum dots (QDs) stand out as an attractive solution for generating quantum light, leveraging their capability for on-demand photon production with high efficiency, and their seamless integration with existent semiconductor foundry processes [3,4]. Beyond deterministic single photon emission, QDs exhibit the remarkable ability to generate polarization-entangled photon pairs on-demand through the biexciton (XX) – exciton (X) recombination cascade [3,4]. However, the effective utilization of QD-based entangled sources in communication technologies encounters challenges, specifically in overcoming the difficulty of finding an efficient emitter that can generate highly entangled photon pairs and ensuring compatibility with the optical fiber transmission windows [5,6].

Self-assembled InAs QDs on GaAs platform emitting in the O-band (around 1.31 μm) or the C-band (around 1.55 μm) fiber optics transmission windows have been realized [7,8]. Achieving the desired emission wavelength involves employing InGa(Al)As metamorphic buffer layers (MMBLs) to red-shift the emission and reduce the number of defects acting as non-radiative recombination centers between QD and barrier layers [5,6,8–13].

Reproducible entangled photon generation requires addressing in-plane anisotropy, such as shape and composition variations, inducing a fine structure splitting (FSS) between bright exciton states through the electron–hole exchange interaction [3,4]. Notably, (111)-oriented surfaces with C_{3v} symmetry gained attention for creating highly symmetrical QDs that can eliminate the FSS of the exciton state [14–17].

However, growing QDs on (111)-oriented surfaces is not straightforward. The commonly employed Stranski–Krastanov growth mode is ineffective due to the rapid plastic relaxation of compressive strain on GaAs(111) substrates which results in the insertion of misfit dislocations at the interface [18,19]. Tensile strain in the epilayers [20,21] or the Droplet Epitaxy (DE) [16,17,22–27] present alternative approaches, offering a more efficient and reliable method of obtaining self-assembled QDs on (111) substrates.

A different effective approach for fabricating high-yield quantum emitters based on QDs is the Local Droplet Etching (LDE) [28–33]. In LDE, the deposition of group III atoms under a low flux of group V atoms leads to the formation of droplets and, subsequently, nanopits underneath the droplet position. Then these nanopits can be subsequently filled with an appropriate semiconductor material to obtain the desired QDs. LDE is performed at higher temperatures with respect to DE. Therefore, it has advantages in terms of crystal quality, brightness, and linewidth broadening of the emitters, the latter related to the dynamic Stark effect induced by charging/discharging traps in the barrier [3,4,34]. Also, it was shown that DE InAs QDs grown on

---

* Corresponding author at: Bicocca Quantum Technologies (BiQuTe) center and Materials Science Department, University of Milano-Bicocca, via R. Cozzi 55, Milano, 20126, Italy.
E-mail address: artur.tuktamyshev@unimib.it (A. Tuktamyshev).

InAlAs(111)A MMBL exceeding critical size became plastically relaxed with dislocations which act as non-radiative recombination centers destroying QD emitting properties [35]. Extending this process to MMBLs on (111)-oriented surfaces holds the potential for achieving bright and entangled photon emission in the O- and C-bands.

In this work, we studied in detail the formation of nanopits produced by deposited metal droplets during the annealing process. Our systematic investigation of growth parameters – deposition temperature, metal flux, and total deposited metal – demonstrates a notable degree of control over the self-assembly of nanopits on GaAs(111)A. We validate and extend the model developed by Heyn and coworkers [30], previously conceived for (001)-oriented surfaces, to describe the physical process on (111) surfaces, thereby providing new insights into the model.

2. Materials and methods

Samples were grown in a conventional MBE chamber. Epi-ready undoped semi-insulating GaAs(111)A substrates with a miscut of 2° towards $[\bar{1}\bar{1}2]$ were used. After oxide desorption, monitored by the appearance of (2×2) surface reconstruction by the reflection of high energy electron diffraction (RHEED), the samples were heated up to 600 °C and were kept at this temperature for 5 minutes to fully remove the oxide layer. Then, a 100 nm GaAs buffer layer was grown at 520 °C with a deposition rate of 0.5 monolayers (ML)/s (here and below 1 ML is defined as 6.26×10^{14} atoms/cm^2, which is the site-number density of the unreconstructed GaAs(001) surface). After the GaAs buffer layer, a 100 nm In$_{0.4}$Ga$_{0.6}$As layer was deposited. The formation of the flat In$_{0.4}$Ga$_{0.6}$As MMBL is achieved following the same growth protocol (low temperature (450 °C) and high growth rate (1 ML/s)) used to obtain the InAlAs MMBL on vicinal GaAs(111)A [36].

Then, the nanopit etching process was performed. It consists of two stages: the deposition of Ga at As$_4$ flux followed by the annealing for 5 minutes at the same temperature. For all the samples, the As$_4$ flux during the etching process was set to have a beam equivalent pressure (BEP) of 1×10^{-7} torr. The etching process was carried out at different temperatures T_s (460–580 °C), Ga flux F_{Ga} (0.1–1.0 ML/s), and Ga total amount deposited Θ_{Ga} (3–27 MLs). The Ga deposition step was not started until the background pressure in the chamber reached the level of $\approx 1-3 \times 10^{-7}$ torr.

The sample morphology was analyzed at room temperature by the Veeco Innova atomic force microscope (AFM) in tapping mode using Nanosensors SSS-NCHR sharp silicon tips capable of a lateral resolution of about 2 nm. The samples were mounted to have one of the cleavage edges ($\langle\bar{1}\bar{1}2\rangle$) parallel to the x-scan direction. All AFM scans with different scan ranges have 512×512 pixel resolution, the scan rate was 0.5 Hz. The surface density of nanopits was estimated from three different 5×5 μm^2 AFM scans for each sample, the nanopit sizes were analyzed from 100 pits randomly chosen on 2×2 μm^2 AFM scans. The pit's width was measured as the altitude of the triangle base of the pits in one of the $\langle\bar{1}\bar{1}2\rangle$ directions (see Fig. 1a) parallel to the x-scan direction. The depth was measured as the difference between the lowest point of the pit and the surface level in the topography profile along the altitude of the triangle base (see Fig. 1b).

The nanopit formation conditions for each of the samples are reported in Table 1.

3. Results

To investigate the self-assembly of nanopits through Ga-assisted LDE on vicinal In$_{0.4}$Ga$_{0.6}$As(111)A, we carried out three comprehensive series of experiments. In the initial series, denoted as the *T series* (samples T1–T7), we systematically varied T_s of the nanopit etching process from 460 to 580 °C while maintaining a constant F_{Ga} and Θ_{Ga} (0.5 ML/s and 3 ML, respectively).
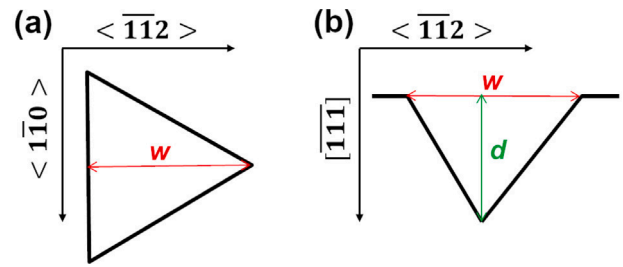

Fig. 1. (a) Schematic representation of the pit's width measurements on AFM scan. (b) Schematic representation of the pit's depth measurements in the profile along the altitude of the triangle base.

Table 1
Description of samples.

Sample	T_s (°C)	Θ_{Ga} (ML)	F_{Ga} (ML/s)	Nanopit density ($\times 10^8$ cm^{-2})
T series:				
T1	460	3	0.5	11.63
T2	480	3	0.5	11.58
T3	500	3	0.5	10.12
T4	520	3	0.5	9.36
T5	540	3	0.5	8.50
T6	560	3	0.5	5.98
T7	580	3	0.5	2.55
F series:				
F1	540	3	0.1	–
F2	540	3	0.2	–
F3	540	3	0.3	6.01
F4=T5	540	3	0.5	8.50
F5	540	3	0.75	11.48
F6	540	3	1.0	12.60
A series:				
A1=F4=T5	540	3	0.5	8.50
A2	540	6	0.5	4.70
A3	540	9	0.5	3.65
A4	540	12	0.5	2.86
A5	540	27	0.5	2.35

Fig. 2 shows the morphological evolution of InGaAs MMBL after the nanopit etching process in the *T series* (samples T1 (460 °C), T3 (500 °C), T5 (540 °C), and T7 (580 °C)). Fig. 3 reports the temperature dependence of the nanopit density and the mean value of the nanopit depth.

Each nanopit exhibits a distinct triangular surface shape, reflecting the symmetry imposed by the (111) growth orientation. The shape of nanopits is discussed in detail in Section 4.4. Although the pit faces do not align with singular facets, the edges of the triangle parallel to $\langle1\bar{1}0\rangle$ directions and symmetrical pit shape indicate a preference to form a tetrahedron by reaching the {111}A facets as in the case of wet etching of GaAs.

The nanopit density is correlated with the density of Ga metal droplets that self-assemble on the surface during the Ga deposition step [28,37]. Due to a thermally activated nature of the droplet self-assembly process [24,38–40], an exponential behavior is expected, characterized by a single activation energy E_N which depends on the barrier energy for the diffusion of Ga adatoms, the critical nucleus size, and the cohesive energy to nucleate critical nucleus ($N \propto \exp[E_N/(k_BT)]$) where k_B is the Boltzmann's constant and T-surface temperature. However, the Arrhenius plot in Fig. 3a reveals a distinct knee at 540 °C, demarcating two regimes.

At lower temperatures, the density dependence, as shown in Fig. 3a, follows to an Arrhenius scaling law with a single activation energy $E_N = 0.24$ eV until approximately 550 °C. Above this point, the density experiences a sharp decline. The average nanopit depth increases with increasing temperature except for the samples grown above 550 °C
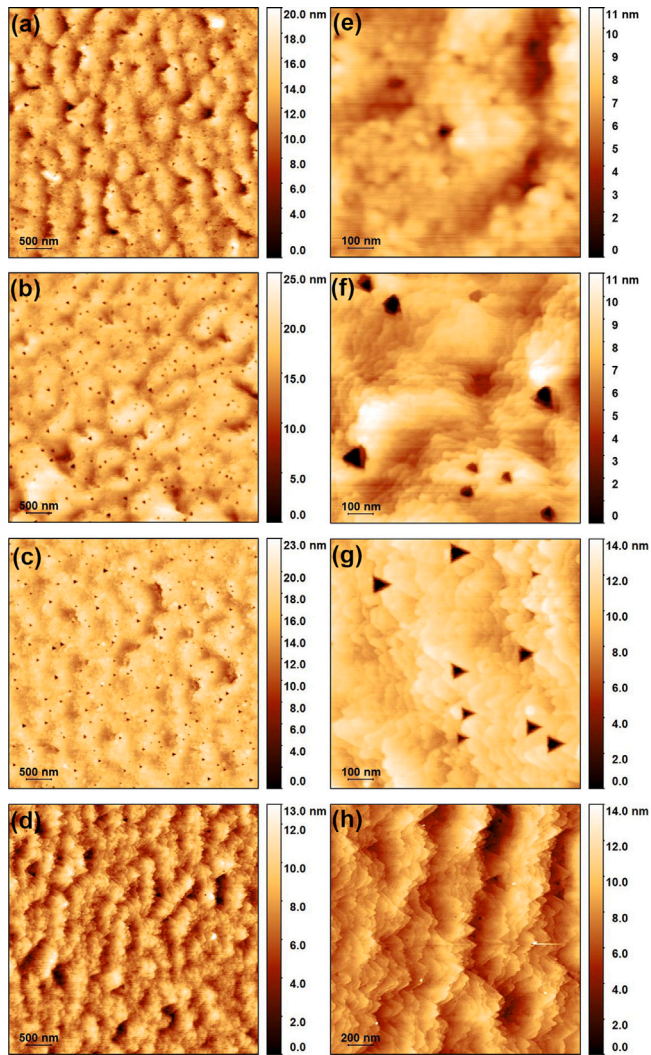
Fig. 2. *T series*: AFM topography images of samples T1 — (a) 5×5 µm², (e) 1×1 µm²; T3 — (b) 5×5 µm², (f) 1×1 µm²; T5 — (c) 5×5 µm², (g) 1×1 µm²; and T7 — (d) 5×5 µm², (h) 2×2 µm².

Fig. 3. *T series*: The temperature dependencies of (a) the nanopit density and (b) the nanopit depth. F_{Ga} and Θ_{Ga} during the fabrication of the sample series are 0.5 ML/s and 3 ML, respectively. Samples T6 and T7 affected by the indium desorption are highlighted by orange points with violet error bars.

(see orange points with violet error bars in Fig. 3). Such a behavior is discussed in Section 4.2.

In the second series (*F series*), F_{Ga} during the droplet deposition step was changed between 0.1 and 1.0 ML/s, while keeping constant $T_s = 540$ °C and $\Theta_{Ga} = 3$ ML. Fig. 4 shows AFM topography images of samples F1 (0.1 ML/s), F3 (0.3 ML/s), and F5 (0.75 ML/s). No nanopit formation is observed for F_{Ga} below 0.3 ML/s. Above 0.3 ML/s the nanopit density follows the expected power dependence on F_{Ga} with the exponent $p = 0.67 \pm 0.06$ (see Fig. 5a). No change in the average depth of nanopits is observed in the whole flux range (Fig. 5b).

In the third series of samples (*A series*), Θ_{Ga} was varied between 3 and 27 MLs while keeping the same $T_s = 540$ °C and F_{Ga} of 0.5 ML/s. Fig. 6 shows the AFM images of samples A1 (3 ML), A3 (9 ML), and A5 (27 ML). It is worth noting that the nanopit density decreases with the increasing Θ_{Ga} or, equivalently, the deposition time (see Fig. 7a). The average depth increases with the increasing Θ_{Ga} (Fig. 7b).

4. Discussion

The droplet etching is one of the possible regimes of the wider droplet-based two-step epitaxy process [25,28,30,41]. After the formation of the nanoscale droplet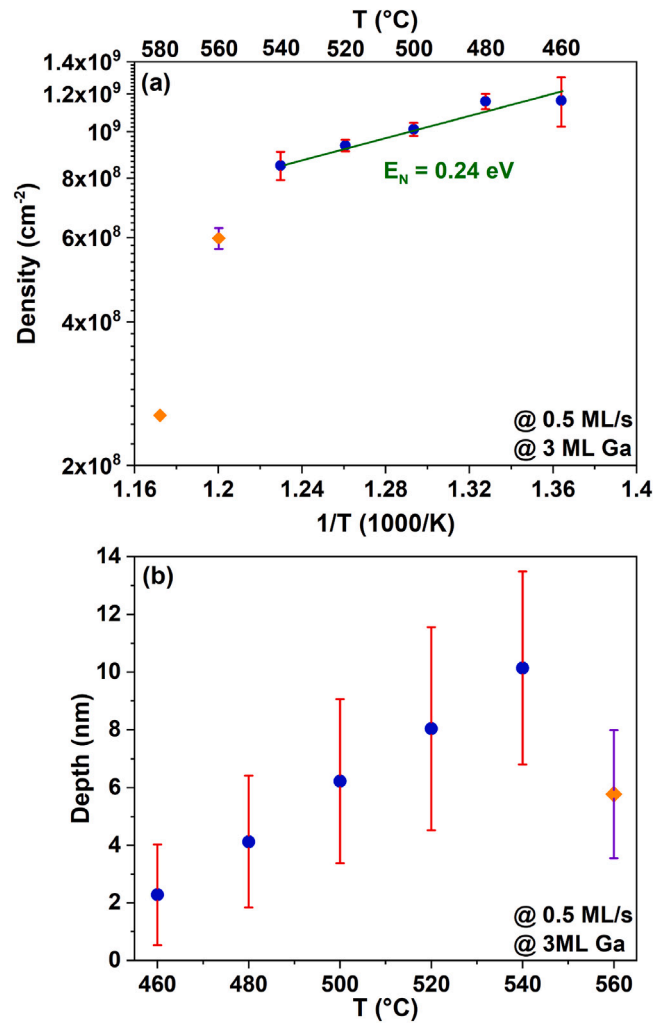s, the conditions used during the annealing step in the group V atmosphere, such as the substrate temperature and the group V flux (arsenic in our case), allow for the self-assembly of three-dimensional nanostructures (called DE process [23,41,42]) or nanopits which constitutes the first step in the QD LDE fabrication process. In the LDE regime, the QDs are then obtained by filling the nanopits with a lower bandgap material. The conditions for DE typically involve an intermediate surface temperature (300–500 °C) and very low group V flux during the droplet deposition step (BEP of about $1 \times 10^{-10} - 1 \times 10^{-9}$ torr) and high group V flux (BEP of about 1×10^{-5} torr) at the same or lower temperature during the annealing step. Conditions for LDE are typically the same for both steps involving high temperature (>500 °C) and an intermediate flux (BEP of about $1 \times 10^{-7} - 1 \times 10^{-6}$ torr) [30,31,43–47].

4.1. The etching model

The observed behavior can be effectively analyzed within the framework established by Heyn and colleagues [30]. This framework integrates island nucleation theory [38,39] with a thermally activated etching process of the III–V semiconductor substrate beneath the droplet by the metal contained in the droplet itself [28]. According to this approach, each nanopit originates from a droplet deposited in the
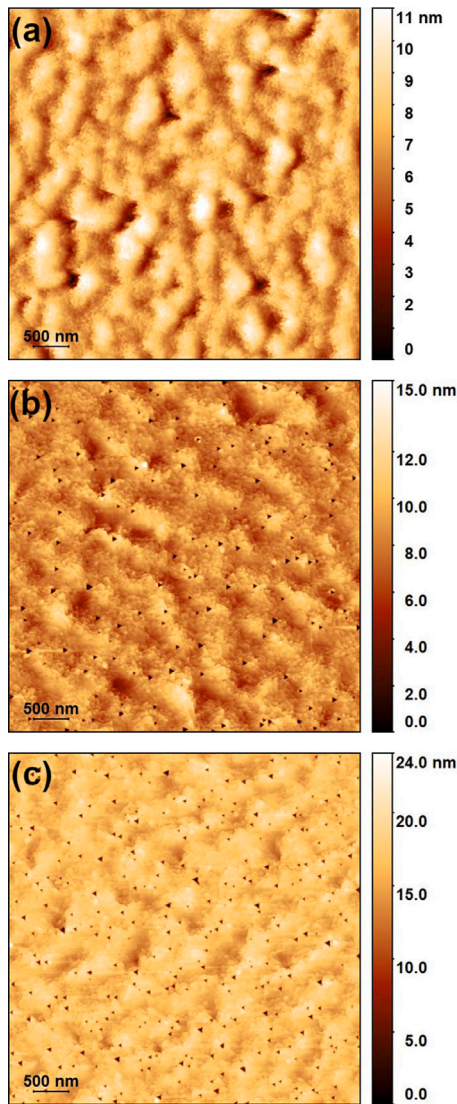
Fig. 4. *F series*: 5 × 5 μm² AFM topography images of samples (a) F1, (b) F3, (c) F5.

Fig. 5. *F series*: The flux dependencies of (a) the nanopit density and (b) the nanopit depth. T_s and Θ_{Ga} during the fabrication of the sample series are 540 °C and 3 ML, respectively.

initial stage of the etching process and it is formed beneath the original droplet position. Both the width and depth of the nanopit are linked to the initial droplet volume and the specifics of the annealing conditions. The droplet ripening process can happen and affect the final density of the nanopits and their size while the etching model remains unchanged [28,29,42]. Moreover, for GaAs(111)A substrates we already demonstrated the negligible effect of the ripening process during DE [27]. In the current study, the ripening was only observed at extremely large Θ_{Ga} as discussed in Section 4.3.

The model built upon these assumptions not only describes the dynamics of the nanopit etching process by the metal within the droplet but also facilitates the identification of potential regimes for nanopit formation. Moreover, it provides a means to engineer the actual shape of the resulting nanopits.

The etching is achieved after the nucleation of droplets by their annealing in a small background flux of group V adatoms (As₄ in the present work, $F_{As_4} > 0$) and zero flux of group III adatoms (Ga in the present work, $F_{Ga} = 0$). The presence of the droplet destabilizes the III–V crystal underneath which starts to dissolve in Ga, In, and As adatoms. The etching is a thermally activated process whose etching rate can be expressed as $R_E = \nu_E \cdot exp[-E_E/(k_BT)]$, where ν_E is a vibrational frequency, E_E is the activation energy for the MMBL
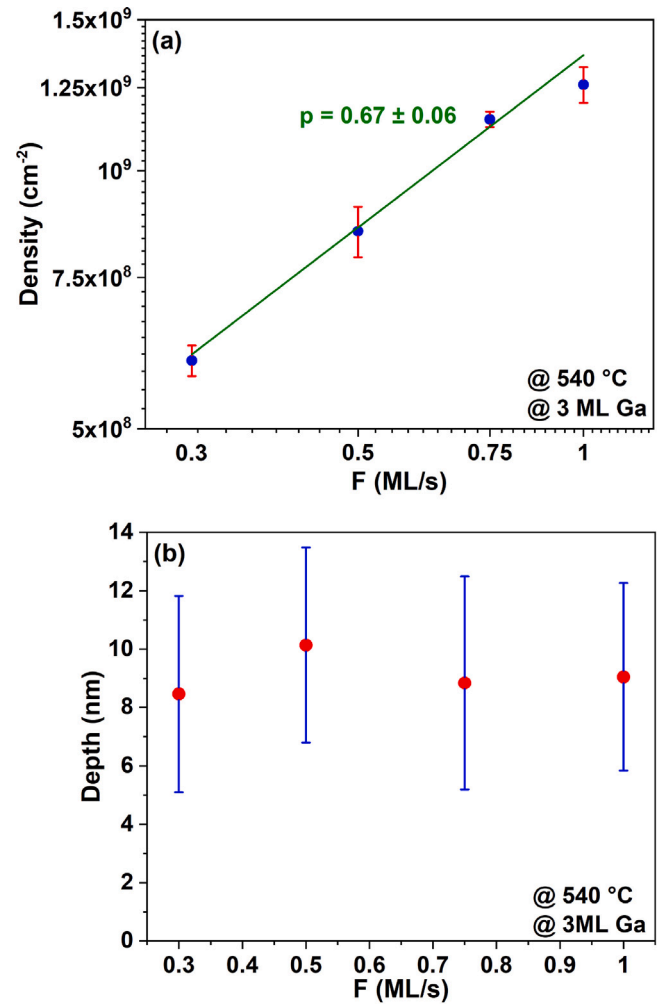
layer etched by Ga. The As dissolved in the droplet during the etching process recrystallizes at the droplet edge (the triple-line) in the form of (In)GaAs or evaporates from the surface.

The etching process remains active until the droplet is fully depleted from its metal atoms. As a matter of fact, there is a net group III adatom flux leaving the droplet by detachment from the droplet perimeter. It is generated by the change in surface tension around the droplet due to the As flux. The detachment is a thermally activated process as well, with the probability $R_D = \nu_D \cdot exp[-E_D/k_BT]$ where ν_D is a vibrational frequency, E_D is the activation energy for group III adatom detachment. Adatoms, after leaving the droplet, react with the As on the surface and are incorporated into the crystal. Therefore, the nanodroplet volume evolution can be described as determined by the Ga adatoms detachment rate R_D. Due to the loss of Ga atoms by detachment from the droplet perimeter, the volume of the droplet V decreases during the annealing: $dV/dt = -V^{1/3}R_D$. This sets the droplet lifetime t_R, together with the boundary conditions $V(t_R) = 0$ (the metal in the droplet fully depleted) $V(0) = \theta/N$, the initial droplet volume, where θ is the metal coverage and N is the droplet density. The latter, according to island nucleation theory, follows the law: $N \propto exp[-E_N/(k_BT)]$. As a consequence, $t_R = C_R \cdot V(0)^{2/3}/R_D$, where C_R being a constant. Therefore, the average nanopit depth d etched below the nanodroplets during the lifetime t_R is:

$$d = R_E t_R = C_R V(0)^{2/3} \frac{R_E}{R_D} \ . \tag{1}$$
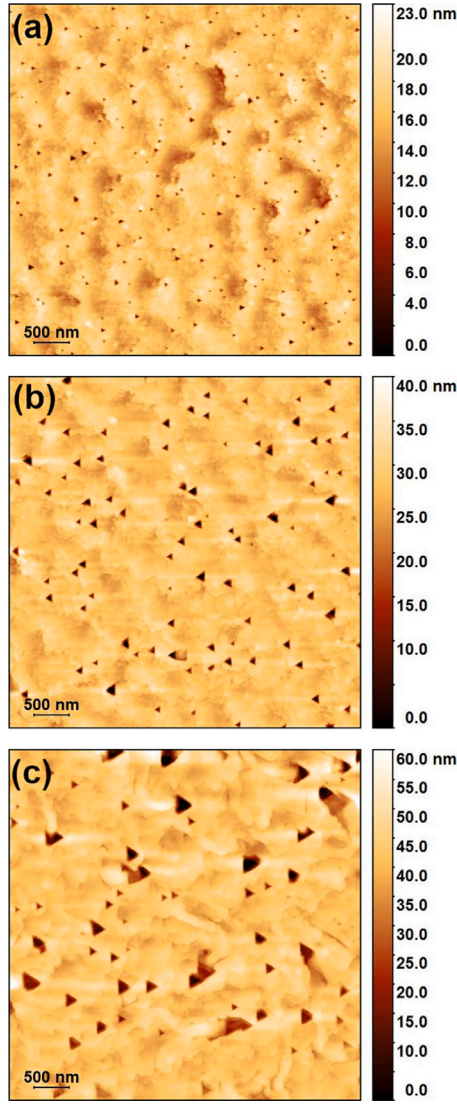
Fig. 6. *A series*: 5 × 5 μm² AFM topography images of samples (a) A1, (b) A3, (c) A5.

Fig. 7. *A series*: the dependencies of (a) the nanopit density and (b) the nanopit depth on Θ_{Ga}. T_s and F_{Ga} during the fabrication of the sample series are 540 °C and 0.5 ML/s, respectively.

We can extend the model to include prediction on the actual aspect ratio AR (depth/width) of the nanopit. The electronic structure of the QDs, fabricated by infilling the nanopits, is strongly influenced by the AR of the pits. Taking into account that the nanopit is starting to form from the droplet edge and the droplet diameter D depends on $V(0)$ as $D = \alpha V(0)^{1/3}$, where α is defined by the actual wetting angle of the droplet, we derive the AR of the nanopit:

$$AR = \frac{d}{D} = \frac{C_R V(0)^{2/3}}{\alpha V(0)^{1/3}} \frac{R_E}{R_D} = C_R \frac{D}{\alpha^2} \cdot \exp[-(E_E - E_D)/k_B T] = C_1(T) \cdot D$$

(2)

Here, term $C_1(T)$ depends on the substrate temperature T:

$$C_1(T) = \frac{C_R}{\alpha^2} \cdot \exp[-(E_E - E_D)/k_B T] = C_2 \cdot \exp[-E_A/k_B T].$$

(3)

where $C_2 = C_R/\alpha^2$ is a constant and E_A is a difference between etching and diffusion activation energies.

4.2. Temperature series

The temperature-dependent nanopit density reveals a deviation in the slope of the Arrhenius plot (see Fig. 3a), indicating the involvement
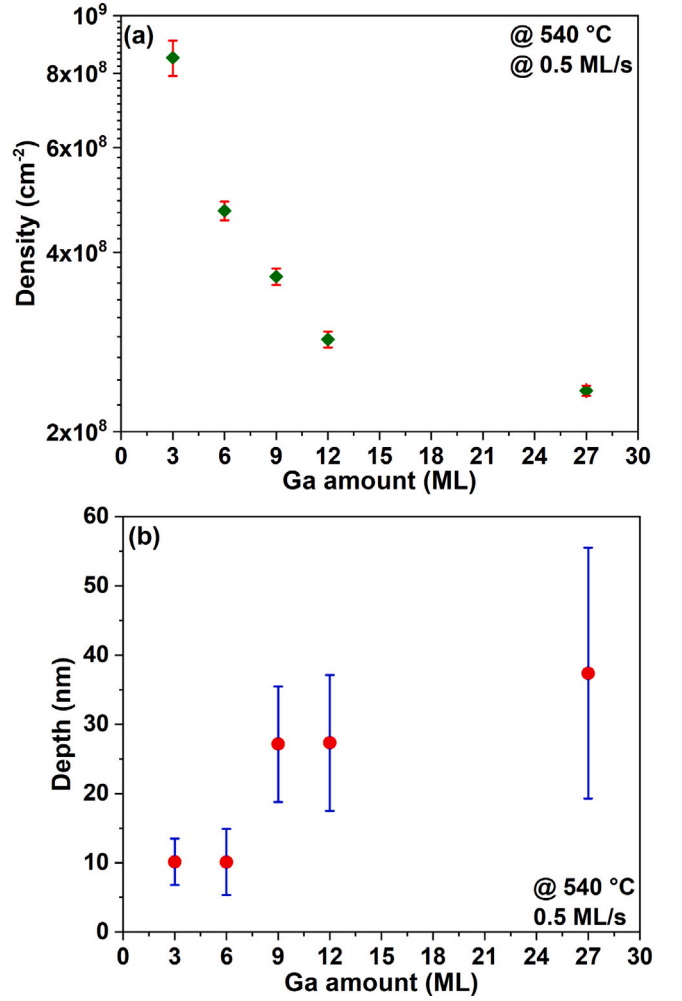
of additional factors in determining nanopit formation. The substantial reduction in nanopit/dot density with increasing temperature, as observed above 550 °C, has previously been attributed to the Ostwald ripening effect or droplet coalescence [31,37,42,48]. In both cases larger droplets are expected, thus leading to deeper nanopit formation [30]. In our case, the sharp change in density above 550 °C is linked to a reduction in nanopit depth (see Fig. 3b). Notably, for sample T7 grown at 580 °C, the nanopit depth dips below 1 nm, making reliable statistical analysis challenging. This unusual behavior may originate from surface roughening of the InGaAs MMBL, induced by intense indium desorption at such elevated temperatures [49]. This surface roughening significantly impacts the dynamics of adatom incorporation and, in turn, droplet formation. Samples affected by the indium desorption (T6 and T7) are highlighted by orange in Fig. 3.

In the temperature range of 460–540 °C, the measured activation energy of the nanopit density is $E_N = 0.24$ eV. This value is notably lower than those observed for nanopit formation using Ga droplets on AlGaAs(001) ($E_N = 0.54$ eV [44]) or AlGaSb(001) ($E_N = 0.51$ eV [47]). Moreover, it is significantly lower than the droplet nucleation activation energy of Ga droplets on vicinal ($E_N = 0.47$ eV at low temperature and 1.47 eV at high temperature) [24] and singular ($E_N = 1.13$ eV) [27] GaAs(111)A. The lower E_N value between droplets and nanopits is related to the presence of an adatom leakage channel related to the presence of an As background. A substantial fraction of
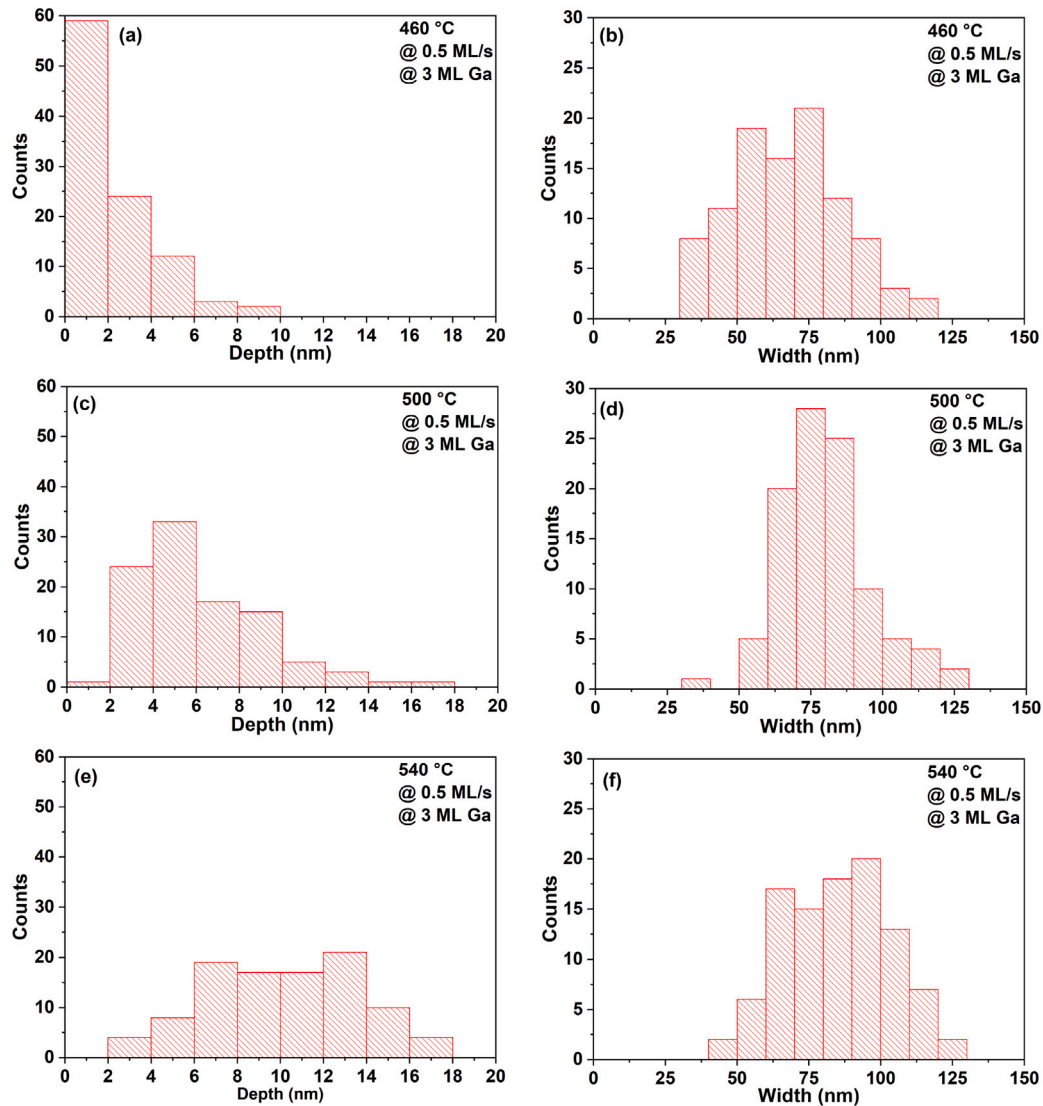
Fig. 8. Depth and width distributions of nanopits of samples (a)–(b) T1, (c)–(d) T3, and (e)–(f) T5.

the deposited Ga adatoms is incorporated in the substrate by reaction with the active As sites induced by As adsorption, thus changing the deposition conditions from complete condensation, as in the case of droplet deposition in Refs. [24,27], to incomplete condensation [50]. An additional contribution to E_N reduction could be attributed to the presence of indium in the MMBL layer, which allows for a decrease in diffusion activation energy [51]. A closer examination calls for an additional process for the reduction in E_N compared to those related to Ga droplet nucleation on GaAs(111)A.

Fig. 8 shows the nanopit depth and width distributions of samples T1, T3, and T5. The nanopit width distributions exhibit a moderate shift in their centroid, from 85 to 65 nm, as the temperature decreases from 540 °C to 460 °C (see Figs. 8b, d, f). This aligns with the observation that substantial changes in droplet volumes have a minor effect on droplet radius. The anticipated change in nanopit width D over the entire temperature range is negligible, as $D \propto V(0)^{1/3} = \alpha(\theta/N)^{1/3}$ [30], and the measured density decreases by 1.4 times from 460 to 540 °C. Therefore, the expected width should increase by only $\sqrt[3]{1.4} = 1.12$ times, consistent with our data.

Conversely, the depth distributions undergo a more pronounced relative shift towards lower values at lower temperatures, with an average value decreasing from 10 at 540 °C to 4 nm at 460 °C. This aligns with expectations from the thermally activated droplet etching process

(Eq. (1)). However, the reduced etching rate influences the nanopit depth distribution, altering its shape and progressively eliminating its shallow tail, as such low nanopit depth becomes comparable with the surface roughness. This effect causes the measured nanopit density at low temperatures to be lower than the actual droplet density, as shallower nanopits remain undetected. The phenomenon contributes to reducing the actual nanopit density, thus resulting in a decrease in the measured density and the E_N value as well.

According to Eq. (2), AR should depend linearly on their width D. The AR dependence on D at different temperatures is reported in Fig. 9. Due to the noisy distribution of the original data, the reported values are the averages of the AR of the nanopits falling into different bins. The bin size is 20 nm, spanning from 0 to 250 nm. Moreover, if inside the bin there were fewer than three data points, it was not considered statistically reliable and not included in the final analysis. The AR data show that the linear dependence on D is maintained in the whole temperature range. The $C_1(T)$ coefficient of the linear interpolation of the data is reported in Table 2. By plotting the temperature dependence of $C_1(T)$ (see Fig. 9b), we calculated the difference between etching and diffusion activation energies $E_E - E_D \approx 0.5$ eV. The AR fit permits disentangling the activation energy of the etching process from that of the adatom diffusion E_D. Additional measurements of the diffusion activation energy (see. e.g. [24,52,53]) would permit to disentangle the two phenomena.
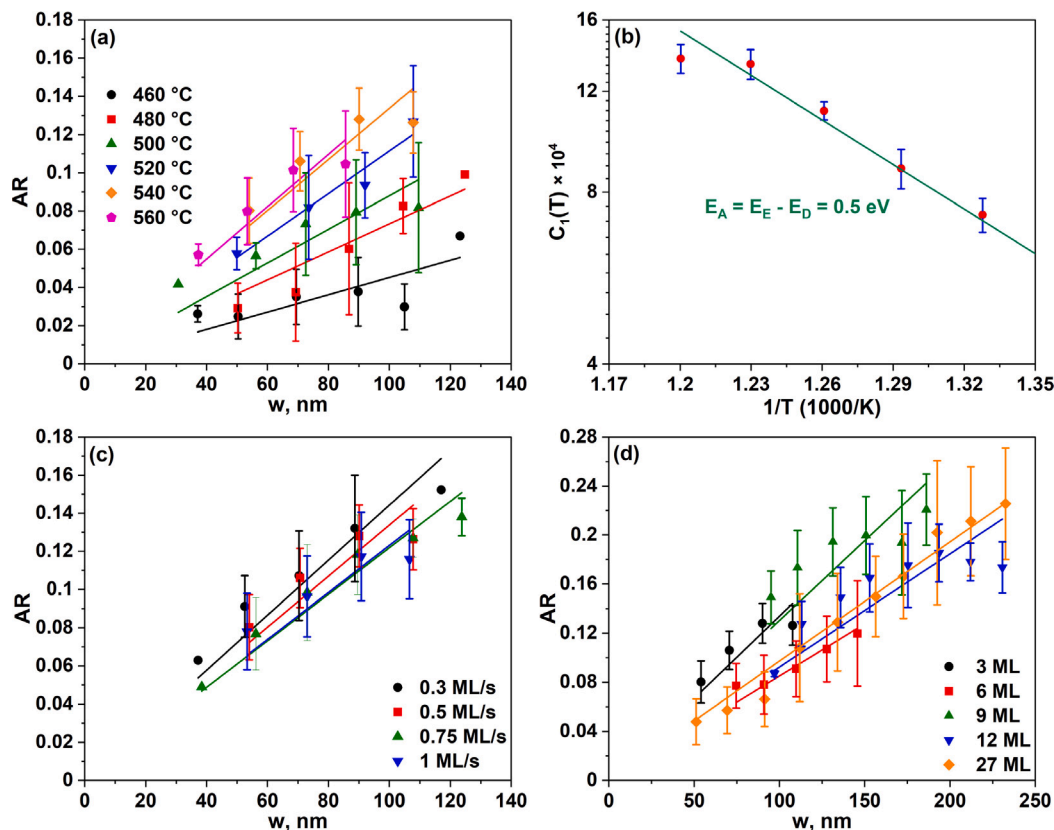
Fig. 9. (a) AR dependence on nanopit width for *T series* samples. (b) Temperature dependence of $C_1(T)$. (c) AR dependence on nanopit width for *F series* samples. (d) AR dependence on nanopit width for *A series* samples.

Table 2
$C_1(T)$ of samples T1–T6.

Sample	$C_1(T) \cdot 10^4$
T1 (460 °C)	4.5 ± 0.5
T2 (480 °C)	7.3 ± 0.5
T3 (500 °C)	8.8 ± 0.7
T4 (520 °C)	11.1 ± 0.4
T5 (540 °C)	13.4 ± 0.8
T6 (560 °C)	13.7 ± 0.8

4.3. Ga flux and Ga amount dependence

The selection of the temperature of 540 °C for the Ga flux and Ga amount series was deliberate, as it allows, according to *T series*, for the optimal achievement of the largest AR within the temperature range studied. This facilitates a more straightforward observation of the nanopit formation.

In the Ga flux series, samples F1 and F2, processed with a Ga flux below 0.3 ML/s, exhibit no measurable nanopit formation on the surface (refer to Fig. 4a). According to basic calculations [54], the As$_4$ flux during the nanopit etching process in this work (BEP $\approx 1 \times 10^{-7}$ torr) is equivalent to 0.2 ML/s. Consequently, all the Ga adatoms deposited in F1 and F2 are incorporated into the surface, and the droplet formation is suppressed. At higher Ga flux levels, nanopits are observed.

Fig. 5b shows that there is no visible alteration in the average nanopit depth, indicating the thermally activated nature of the nanopit formation process. The density of these nanopits scales by a factor of 2.1 between sample F3 (0.3 ML/s) and sample F6 (1 ML/s). Applying classical nucleation theory [24,39,50], where the droplet density is expressed as a power dependence, $N \propto F^p$, the exponent p can be estimated from the observed Ga flux dependence data (refer to Fig. 5a):

$p = 0.67 \pm 0.06$. Considering the high Ga flux and temperature during Ga deposition, it becomes feasible to estimate the critical cluster size i [24,39,50]. By accounting for initially incomplete condensation [50], as the presence of the background As pressure introduce a loss channel in the adatom density, the relationship $p = 2i/5$ yields $i = 5p/2 = 1.675 \pm 0.150$. This estimate aligns with findings from previous works [24,27].

Surface topography analysis indicates that the nanopit density decreases with the increasing Ga coverage Θ_{Ga}, as shown in Fig. 7a. This phenomenon is ascribed to the Ostwald ripening [42,55] and coalescence of droplets due to droplet motion [56] during Ga deposition, the latter evidenced by the presence of trenches following droplet movements and the fusion of multiple nanopits. The coalescence process results in an increase in droplet sizes, thus influencing the sizes of nanopits and causing an increase in the width of the size distribution (Fig. 7b).

The AR dependence for both *F* and *A series* samples (see Figs. 9c and d) reveals a consistent trend: there is no discernible change in the linear coefficient $C_1(T)$ depending on F_{Ga} and Θ_{Ga}. Despite the huge change in the nanopit size, AR still shows a linear dependence on the droplet diameter with a coefficient that depends solely on the crystallization temperature.

4.4. Nanopit shape

The morphology of nanopits on the (111)-oriented surface closely adheres to its inherent symmetry, as illustrated in Fig. 10. These nanopits exhibit a pyramid shape with an equilateral triangle base, where the edges of the triangle align parallel to the $\langle 1\bar{1}0 \rangle$ directions. The high degree of symmetry is evident in the topography profiles of individual pits, as depicted in Fig. 10b. Notably, the specific facets of these inverted pyramids remain undetermined due to the variability in depth achievable with the same base size, as discussed in Section 4.2.
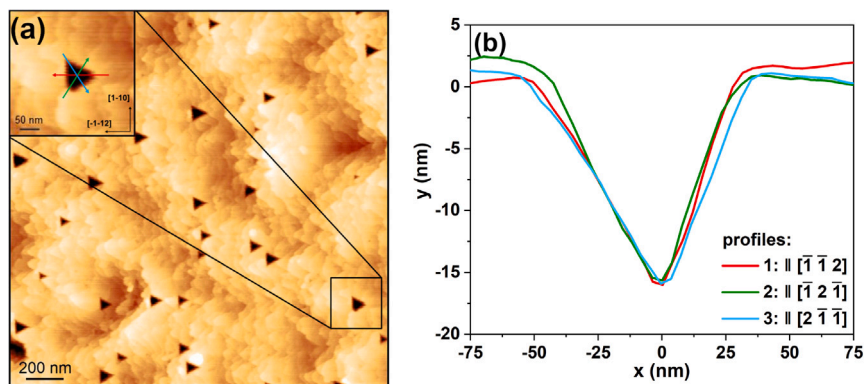
Fig. 10. (a) 2×2 µm² AFM topography image of sample T5. The inset shows a magnified image of a single pit. (b) Topography profiles of a single pit in the inset in (a) taken parallel to $\langle \bar{1}\bar{1}2 \rangle$ directions.

These triangular pyramids bear a resemblance to V-grooves and inverted pyramids formed through a wet chemical etching process on GaAs(111)B substrates [57]. However, in the wet etching, the facets of the pyramids are determined by the (111)A surfaces. This is attributed to the etchant encountering (111)A surfaces, resulting in a substantial reduction in the etching rate. In the nanopit etching by droplet, a similar expectation exists for the pyramids to reach (111)A facets; however, the etching rate is slow, and the available droplet material is insufficient to attain these facets.

A notable distinction in the etched nanopits on the (111) surface is the absence of an outer ring or disk nanostructure around each pit, in contrast to the (001)-oriented surface [29–33,37,43–47]. The formation of the ring-like nanostructure in the latter case is attributed to the (111)-front direction of GaAs crystallization initiating from the droplet edge, inclined at a 55° angle to the (001) direction [58,59]. Conversely, on the (111)-oriented surface, the epilayer growth direction coincides with the liquid-crystal interface growth direction. This alignment results in adatom diffusion and absorption by kinks and step edges, which are more prevalent on the (111)-oriented surface, especially on the vicinal one.

5. Conclusions

The presented study provides a comprehensive analysis of the etched nanopit formation by Ga droplets on (111)-oriented surfaces in the context of InGaAs MMBL. The investigation spans a range of experimental conditions, including T_s, F_{Ga}, and Θ_{Ga} variations.

The observed nanopit morphology, featuring pyramid-shaped structures with equilateral triangle bases, aligns with the inherent symmetry of the (111)-oriented surface. The absence of an outer ring or disk nanostructure distinguishes these nanopits from their counterparts on (001)-oriented surfaces. The unique geometric characteristics are attributed to the interplay between the droplet-based etching process and the crystallographic orientation of the substrate.

The proposed etching model in this study, built upon the work of Heyn and colleagues [30], successfully integrates island nucleation theory with the thermally activated etching process. The model elucidates the dynamics of nanopit formation, including aspects such as droplet nucleation, substrate etching, and adatom detachment from the droplets. The resulting equations facilitate predictions of nanopit depth, width, and aspect ratio based on the experimental parameters. In particular, we extended the model to predict the nanopit AR dependence on droplet size at different deposition conditions.

Temperature-dependent studies of the nanopit density reveal a deviation in the Arrhenius plot, suggesting additional factors influencing nanopit formation, such as Ostwald ripening, coalescence, droplet motion, and surface roughening at high temperatures. The activation energy for nanopit density is determined to be $E_N = 0.24$ eV in the temperature range of 460–540 °C, a value notably lower than those reported for droplet formation on other substrates. We interpreted such reduction as stemming from the combined effect of the incomplete condensation regime and of the limited etching that takes place at low T_s and reduces the measurable nanopit density with respect to the pristine droplet density.

F_{Ga} and Θ_{Ga} series further demonstrate the interplay between experimental parameters and nanopit characteristics. The absence of nanopits at low Ga flux is attributed to Ga adatom incorporation into the substrate, preventing droplet formation. The density and size of nanopits increase with higher F_{Ga}, showcasing the significance of droplet availability in the etching process. The AR of nanopits remains linearly dependent on droplet width across different temperatures, F_{Ga} and Θ_{Ga}, revealing a consistent relationship in agreement with the presented model. The linear coefficient $C_1(T)$ in this relationship is found to be dependent solely on the substrate temperature, providing insights into the thermally activated nature of the etching process.

In summary, this work contributes to the understanding of the nanopit formation process on (111)-oriented surfaces and offers valuable insights into the intricate interplay between experimental conditions and resulting nanostructures. The proposed etching model provides a framework for predicting and engineering nanopit characteristics, facilitating advancements in the field of semiconductor quantum dot fabrication through LDE.

CRediT authorship contribution statement

Artur Tuktamyshev: Writing – original draft, Visualization, Validation, Supervision, Methodology, Investigation, Formal analysis, Conceptualization. **Davide Lambardi:** Writing – original draft, Visualization, Methodology, Investigation, Formal analysis. **Stefano Vichi:** Writing – review & editing, Validation, Investigation, Formal analysis. **Federico Cesura:** Writing – review & editing, Validation. **Stefano Cecchi:** Writing – review & editing, Validation. **Alexey Fedorov:** Writing – review & editing, Validation, Investigation. **Sergio Bietti:** Writing – review & editing, Validation, Investigation. **Stefano Sanguinetti:** Writing – review & editing, Validation, Supervision, Resources, Project administration, Methodology, Funding acquisition, Conceptualization.

Declaration of competing interest

The authors declare that they have no known competing financial interests or personal relationships that could have appeared to influence the work reported in this paper.

Data availability

Data will be made available on request.

References

[1] N. Gisin, G. Ribordy, W. Tittel, H. Zbinden, Quantum cryptography, Rev. Mod. Phys. 74 (2002) 145–195, http://dx.doi.org/10.1103/RevModPhys.74.145.

[2] H.J. Kimble, The quantum internet, Nature 453 (2008) 1023–1030, http://dx.doi.org/10.1038/nature07127.

[3] A. Orieux, M.A.M. Versteegh, K.D. Jöns, S. Ducci, Semiconductor devices for entangled photon pair generation: a review, Rep. Progr. Phys. 80 (2017) 076001, http://dx.doi.org/10.1088/1361-6633/aa6955.

[4] D. Huber, M. Reindl, J. Aberl, A. Rastelli, R. Trotta, Semiconductor quantum dots as an ideal source of polarization-entangled photon pairs on-demand: a review, J. Opt. 20 (2018) 073002, http://dx.doi.org/10.1088/2040-8986/aac4c4.

[5] S.L. Portalupi, M. Jetter, P. Michler, InAs quantum dots grown on metamorphic buffers as non-classical light sources at telecom C-band: a review, Semicond. Sci. Technol. 34 (2019) 053001, http://dx.doi.org/10.1088/1361-6641/ab08b4.

[6] Y. Yu, S. Liu, C.-M. Lee, P. Michler, S. Reitzenstein, K. Srinivasan, E. Waks, J. Liu, Telecom-band quantum dot technologies for long-distance quantum networks, Nature Nanotechnol. 18 (2023) 1389–1400, http://dx.doi.org/10.1038/s41565-023-01528-7.

[7] M.B. Ward, O.Z. Karimov, D.C. Unitt, Z.L. Yuan, P. See, D.G. Gevaux, A.J. Shields, P. Atkinson, D.A. Ritchie, On-demand single-photon source for 1.3 μm telecom fiber, Appl. Phys. Lett. 86 (2005) 201111, http://dx.doi.org/10.1063/1.1922573.

[8] M. Paul, F. Olbrich, J. Höschele, S. Schreier, J. Kettler, S.L. Portalupi, M. Jetter, P. Michler, Single-photon emission at 1.55 μm from MOVPE-grown InAs quantum dots on InGaAs/GaAs metamorphic buffers, Appl. Phys. Lett. 111 (2017) 033102, http://dx.doi.org/10.1063/1.4993935.

[9] L. Seravalli, M. Minelli, P. Frigeri, S. Franchi, G. Guizzetti, M. Patrini, T. Ciabattoni, M. Geddo, Quantum dot strain engineering of InAs/InGaAs nanostructures, J. Appl. Phys. 101 (2007) 024313, http://dx.doi.org/10.1063/1.2424523.

[10] N. Ha, T. Mano, T. Kuroda, K. Mitsuishi, A. Ohtake, A. Castellano, S. Sanguinetti, T. Noda, Y. Sakuma, K. Sakoda, Droplet epitaxy growth of telecom InAs quantum dots on metamorphic InAlAs/GaAs(111)A, Japan. J. Appl. Phys. 54 (2015) 04DH07, http://dx.doi.org/10.7567/JJAP.54.04DH07.

[11] W. Zhan, S. Ishida, J. Kwoen, K. Watanabe, S. Iwamoto, Y. Arakawa, Emission at 1.6 μm from InAs quantum dots in metamorphic InGaAs matrix, Phys. Status Solidi B 257 (2020) 6710–6716, http://dx.doi.org/10.1002/pssb.201900392.

[12] A. Tuktamyshev, A. Fedorov, S. Bietti, S. Vichi, K.D. Zeuner, K.D. Jöns, D. Chrastina, S. Tsukamoto, V. Zwiller, M. Gurioli, S. Sanguinetti, Telecom-wavelength InAs QDs with low fine structure splitting grown by droplet epitaxy on GaAs(111)A vicinal substrates, Appl. Phys. Lett. 118 (2021) 133102, http://dx.doi.org/10.1063/5.0045776.

[13] A. Barbiero, A. Tuktamyshev, G. Pirard, J. Huwer, T. Müller, R.M. Stevenson, S. Bietti, S. Vichi, A. Fedorov, G. Bester, S. Sanguinetti, A.J. Shields, Exciton fine structure in InAs quantum dots with cavity-enhanced emission at telecommunication wavelength and grown on a GaAs(111)A vicinal substrate, Phys. Rev. Appl. 18 (2021) 034081, http://dx.doi.org/10.1103/PhysRevApplied.18.034081.

[14] R. Singh, G. Bester, Nanowire quantum dots as an ideal source of entangled photon pairs, Phys. Rev. Lett. 103 (2009) 063601, http://dx.doi.org/10.1103/PhysRevLett.103.063601.

[15] A. Schliwa, M. Winkelnkemper, A. Lochmann, E. Stock, D. Bimberg, In(Ga)As/GaAs quantum dots grown on a (111) surface as ideal sources of entangled photon pairs, Phys. Rev. B 80 (2009) http://dx.doi.org/10.1103/PhysRevB.80.161307, 161307(R).

[16] T. Mano, M. Abbarchi, T. Kuroda, B. McSkimming, A. Ohtake, K. Mitsuishi, K. Sakoda, Self-assembly of symmetric GaAs quantum dots on (111)A substrates: suppression of fine-structure splitting, Appl. Phys. Express 3 (2010) 065203, http://dx.doi.org/10.1143/APEX.3.065203.

[17] F. Basso Basset, S. Bietti, M. Reindl, L. Esposito, A. Fedorov, D. Huber, A. Rastelli, E. Bonera, R. Trotta, S. Sanguinetti, High-yield fabrication of entangled photon emitters for hybrid quantum networking using high-temperature droplet epitaxy, Nano Lett. 18 (2018) 505–512, http://dx.doi.org/10.1021/acs.nanolett.7b04472.

[18] H. Yamaguchi, J.G. Belk, X.M. Zhang, J.L. Sudijono, M.R. Fahy, T.S. Jones, D.W. Pashley, B.A. Joyce, Atomic-scale imaging of strain relaxation via misfit dislocations in highly mismatched semiconductor heteroepitaxy: InAs/GaAs(111)A, Phys. Rev. B 55 (1997) 1337–1340, http://dx.doi.org/10.1103/PhysRevB.55.1337.

[19] H. Wen, Z.M. Wang, J.L. Shultz, B.L. Liang, G.J. Salamo, Growth and characterization of InAs epitaxial layer on GaAs(111)B, Phys. Rev. B 70 (2004) 205307, http://dx.doi.org/10.1103/PhysRevB.70.205307.

[20] C.D. Yerino, P.J. Simmonds, B. Liang, D. Jung, C. Schneider, S. Unsleber, M. Vo, D.L. Huffaker, S. Höfling, M. Kamp, M.L. Lee, Strain-driven growth of GaAs(111) quantum dots with low fine structure splitting, Appl. Phys. Lett. 105 (2014) 251901, http://dx.doi.org/10.1063/1.4904944.

[21] C.F. Schuck, R.A. McCown, A. Hush, A. Mello, S. Roy, J.W. Spinuzzi, B. Liang, D.L. Huffaker, P.J. Simmonds, Self-assembly of (111)-oriented tensile-strained quantum dots by molecular beam epitaxy, J. Vac. Sci. Technol. B 36 (2018) 031803, http://dx.doi.org/10.1116/1.5018002.

[22] T. Kuroda, T. Mano, N. Ha, H. Nakajima, H. Kumano, B. Urbaszek, M. Jo, M. Abbarchi, Y. Sakuma, K. Sakoda, I. Suemune, X. Marie, T. Amand, Symmetric quantum dots as efficient sources of highly entangled photons: violation of Bell's inequality without spectral and temporal filtering, Phys. Rev. B 88 (2013) http://dx.doi.org/10.1103/PhysRevB.88.041306, 041306(R).

[23] S. Sanguinetti, S. Bietti, N. Koguchi, Droplet epitaxy of nanostructures, in: M. Henini (Ed.), Molecular Beam Epitaxy: from Research to Mass Production, second ed., Elsevier, 2018, pp. 293–314, http://dx.doi.org/10.1016/B978-0-12-812136-8.00013-X.

[24] A. Tuktamyshev, A. Fedorov, S. Bietti, S. Tsukamoto, S. Sanguinetti, Temperature activated dimensionality crossover in the nucleation of quantum dots by droplet epitaxy on GaAs(111)A vicinal substrates, Sci. Rep. 9 (2019) 14520, http://dx.doi.org/10.1038/s41598-019-51161-5.

[25] M. Gurioli, Z. Wang, A. Rastelli, T. Kuroda, S. Sanguinetti, Droplet epitaxy of semiconductor nanostructures for quantum photonic devices, Nature Mater. 17 (2019) 799–810, http://dx.doi.org/10.1038/s41563-019-0355-y.

[26] S. Bietti, F. Basso Basset, A. Tuktamyshev, E. Bonera, A. Fedorov, S. Sanguinetti, High–temperature droplet epitaxy of symmetric GaAs/AlGaAs quantum dots, Sci. Rep. 10 (2020) 6532, http://dx.doi.org/10.1038/s41598-020-62248-9.

[27] A. Tuktamyshev, A. Fedorov, S. Bietti, S. Vichi, R. Tambone, S. Tsukamoto, S. Sanguinetti, Nucleation of Ga droplets self-assembly on GaAs(111)A substrates, Sci. Rep. 11 (2021) 6833, http://dx.doi.org/10.1038/s41598-021-86339-3.

[28] Z.M. Wang, B.L. Liang, K.A. Sablon, G.J. Salamo, Nanoholes fabricated by self-assembled gallium nanodrill on GaAs(100), Appl. Phys. Lett. 90 (2007) 113120, http://dx.doi.org/10.1063/1.2713745.

[29] C. Heyn, A. Stemmann, T. Köppen, C. Strelow, T. Kipp, M. Grave, S. Mendach, W. Hansen, Highly uniform and strain-free GaAs quantum dots fabricated by filling of self-assembled nanoholes, Appl. Phys. Lett. 94 (2009) 183113, http://dx.doi.org/10.1063/1.3133338.

[30] C. Heyn, T. Bartsch, S. Sanguinetti, D. Jesson, W. Hansen, Dynamics of mass transport during nanohole drilling by local droplet etching, Nanoscale Res. Lett. 10 (2015) 67, http://dx.doi.org/10.1186/s11671-015-0779-5.

[31] C. Heyn, M. Zocher, S. Schnüll, W. Hansen, Role of arsenic during aluminum droplet etching of nanoholes in AlGaAs, Nanoscale Res. Lett. 11 (2016) 428, http://dx.doi.org/10.1186/s11671-016-1648-6.

[32] Y.H. Huo, A. Rastelli, O.G. Schmidt, Ultra-small excitonic fine structure splitting in highly symmetric quantum dots on GaAs (001) substrate, Appl. Phys. Lett. 102 (2013) 152105, http://dx.doi.org/10.1063/1.4802088.

[33] Y.H. Huo, B.J. Witek, S. Kumar, J.R. Cardenas, J.X. Zhang, N. Akopian, R. Singh, E. Zallo, R. Grifone, D. Kriegner, R. Trotta, F. Ding, J. Stangl, V. Zwiller, G. Bester, A. Rastelli, O.G. Schmidt, A light-hole exciton in a quantum dot, Nat. Phys. 10 (2013) 46–51, http://dx.doi.org/10.1038/nphys2799.

[34] F. Basso Basset, S. Bietti, A. Tuktamyshev, S. Vichi, E. Bonera, S. Sanguinetti, Spectral broadening in self-assembled GaAs quantum dots with narrow size distribution, J. Appl. Phys. 126 (2019) 024301, http://dx.doi.org/10.1063/1.5097277.

[35] A. Tuktamyshev, S. Vichi, F. Cesura, A. Fedorov, G. Carminati, D. Lambardi, J. Pedrini, E. Vitiello, F. Pezzoli, S. Bietti, S. Sanguinetti, Strain relaxation of InAs quantum dots on misoriented InAlAs(111) metamorphic substrates, Nanomaterials 12 (2022) 3571, http://dx.doi.org/10.3390/nano12203571.

[36] A. Tuktamyshev, S. Vichi, F. Cesura, A. Fedorov, S. Bietti, D. Chrastina, S. Tsukamoto, S. Sanguinetti, Flat metamorphic InAlAs buffer layer on GaAs(111)A misoriented substrates by growth kinetics control, J. Cryst. Growth 600 (2022) 126906, http://dx.doi.org/10.1016/j.jcrysgro.2022.126906.

[37] C. Heyn, A. Stemmann, W. Hansen, Dynamics of self-assembled droplet etching, Appl. Phys. Lett. 95 (2009) 173110, http://dx.doi.org/10.1063/1.3254216.

[38] J.A. Venables, Atomic processes in crystal growths, Surf. Sci. 299/300 (1994) 798–817, http://dx.doi.org/10.1016/0039-6028(94)90698-X.

[39] T. Michely, J. Krug, Islands, Mounds and Atoms, Springer Berlin Heidelberg, 2004, pp. 25–29, http://dx.doi.org/10.1007/978-3-642-18672-1.

[40] A. Tuktamyshev, A. Fedorov, S. Bietti, S. Tsukamoto, R. Bergamaschini, F. Montalenti, S. Sanguinetti, Reentrant behavior of the density vs. temperature of indium islands on GaAs(111)A, Nanomaterials 10 (2020) 1512, http://dx.doi.org/10.3390/nano10081512.

[41] N. Koguchi, S. Takahashi, T. Chikyow, New MBE growth method for InSb quantum well boxes, J. Cryst. Growth 111 (1991) 688–692, http://dx.doi.org/10.1016/0022-0248(91)91064-H.

[42] C. Heyn, A. Stemmann, A. Schramm, H. Welsch, W. Hansen, Regimes of GaAs quantum dot self-assembly by droplet epitaxy, Phys. Rev. B 76 (2007) 075317, http://dx.doi.org/10.1103/PhysRevB.76.075317.

[43] C. Heyn, A. Stemmann, W. Hansen, Nanohole formation on AlGaAs surfaces by local droplet etching with gallium, J. Cryst. Growth 311 (2009) 1839–1842, http://dx.doi.org/10.1016/j.jcrysgro.2008.11.001.

[44] C. Heyn, Kinetic model of local droplet etching, Phys. Rev. B 83 (2011) 165302, http://dx.doi.org/10.1103/PhysRevB.83.165302.

[45] D. Sonnenberg, A. Graf, V. Paulava, W. Hansen, C. Heyn, Highly versatile ultra-low density GaAs quantum dots fabricated by filling of self-assembled nanoholes, Appl. Phys. Lett. 101 (2012) 143106, http://dx.doi.org/10.1063/1.4756945.

[46] C. Heyn, S. Schnüll, D.E. Jesson, W. Hansen, Thermally controlled widening of droplet etched nanoholes, Nanoscale Res. Lett. 9 (2014) 285, http://dx.doi.org/10.1186/1556-276X-9-285.

[47] J. Hilska, A. Chellu, T. Hakkarainen, Nanohole etching in AlGaSb with gallium droplets, Cryst. Growth Des. 21 (2021) 1917–1923, http://dx.doi.org/10.1021/acs.cgd.1c00113.

[48] A. Ohtake, N. Ha, T. Mano, Extremely high- and low-density of Ga droplets on GaAs(111)A,B: surface-polarity dependence, Cryst. Growth Des. 15 (2015) 485–488, http://dx.doi.org/10.1021/cg501545n.

[49] K. Radhakrishnan, S.F. Yoon, R. Gopalakrishnan, K.L. Tan, Indium desorption from strained InGaAs/GaAs quantum wells grown by molecular beam epitaxy, J. Vac. Sci. Technol. A 12 (1994) 1124–1128, http://dx.doi.org/10.1116/1.579176.

[50] J. Venables, G. Spiller, M. Hanbucken, Nucleation and growth of thin films, Rep. Progr. Phys. 47 (1984) 399–459, http://dx.doi.org/10.1088/0034-4885/47/4/002.

[51] E. Penev, S. Stojković, P. Kratzer, M. Scheffler, Anisotropic diffusion of In adatoms on pseudomorphic $In_xGa_{1-x}As$ films: first-principles total energy calculations, Phys. Rev. B 69 (2004) 115335, http://dx.doi.org/10.1103/PhysRevB.69.115335.

[52] J.H. Neave, P.J. Dobson, B.A. Joyce, J. Zhang, Reflection high-energy electron diffraction oscillations from vicinal surfaces - a new approach to surface diffusion measurements, Appl. Phys. Lett. 47 (2015) 100–102, http://dx.doi.org/10.1063/1.96281.

[53] S. Bietti, C. Somaschini, L. Esposito, A. Fedorov, S. Sanguinetti, Gallium surface diffusion on GaAs(001) surfaces measured by crystallization dynamics of Ga droplets, J. Appl. Phys. 116 (2014) 114311, http://dx.doi.org/10.1063/1.4895986.

[54] T. Joyce, T. Bullough, Beam equivalent pressure measurements in chemical beam epitaxy, J. Cryst. Growth 127 (1993) 265–269, http://dx.doi.org/10.1016/0022-0248(93)90619-8.

[55] W. Ostwald, Über die vermeintliche Isomerie des roten und gelben Quecksilberoxyds und die Oberflächenspannung fester Körper, Z. Phys. Chem., Stoechiom. Verwandtschaftsl. 34 (1900) 495, http://dx.doi.org/10.1515/zpch-1900-3431.

[56] S. Kanjanachuchai, C. Euaruksakul, Self-running Ga droplets on GaAs (111)A and (111)B surfaces, ACS Appl. Mater. Interfaces 5 (2013) 7709–7713, http://dx.doi.org/10.1021/am402455u.

[57] E. Pelucchi, S. Moroni, V. Dimastrodonato, D. Vvedensky, Self-ordered nanostructures on patterned substrates, J. Mater. Sci.: Mater. Electron. 29 (2018) 952–967, http://dx.doi.org/10.1007/s10854-017-7993-0.

[58] K. Hiruma, M. Yazawa, K. Haraguchi, K. Ogawa, T. Katsuyama, M. Koguchi, H. Kakibayashi, GaAs free-standing quantum-size wires, J. Appl. Phys. 74 (1993) 3162–3171, http://dx.doi.org/10.1063/1.354585.

[59] S. Bietti, C. Somaschini, S. Sanguinetti, Crystallization kinetics of Ga metallic nano-droplets under As flux, Nanotechnology 24 (2013) 205603, http://dx.doi.org/10.1088/0957-4484/24/20/205603.